

Titanium nitride–carbon nanotube core–shell composites as effective electrocatalyst supports for low temperature fuel cells

Drew C. Higgins, Ja-Yeon Choi, Jason Wu, Anand Lopez and Zhongwei Chen*

Received 5th October 2011, Accepted 13th December 2011

DOI: 10.1039/c2jm15014j

Titanium nitride–carbon nanotube (TiN–CNT) core–shell nanocomposites were developed by a simplistic two step fabrication procedure and characterized by transmission electron microscopy, X-ray diffraction and thermogravimetric analysis. These materials were utilized as platinum nanoparticle electrocatalyst supports (Pt/TiN–CNT) for the oxygen reduction reaction (ORR) and methanol oxidation reaction (MOR), two important low temperature fuel cell processes. Improved ORR and MOR activities were demonstrated for Pt/TiN–CNTs compared with state of the art commercial Pt/C. Moreover, enhanced CO tolerance towards the MOR was demonstrated attributed to the interaction occurring between adsorbed CO molecules and the TiN–CNT supports. TiN–CNTs are thus presented as highly promising, novel electrocatalyst support materials with enhanced ORR and MOR performance attributed to their anisotropic morphology, enhanced electronic properties and conductivity, and distinct catalyst–support interactions.

Introduction

The appeal of proton exchange membrane fuel cells (PEMFCs) and direct methanol fuel cells (DMFCs) is steadily increasing globally as a result of the depleting natural fossil fuel reserves and increasing environmental awareness. In order to advance research and development efforts and one day realize a sustainable fuel cell market, improvements in the activity, durability and contaminant tolerance are required for the platinum based electrocatalyst materials utilized to facilitate the respective electrode reactions and generate power at a practical rate. It is well established that these properties are highly dependent on the type of electrocatalyst support material utilized, influenced by their specific nanostructures and catalyst–support interactions.^{1,2} Generally the requirement for catalyst support materials includes high surface areas, electronic conductivity and facile mass transport properties along with a high degree of stability under the conditions encountered during fuel cell operation. Traditionally, microporous carbon blacks are utilized as electrocatalyst support materials for fuel cell reactions, however numerous alternatives have been investigated including various carbon morphologies such as carbon nanotubes^{3–5} and graphene,^{6,7} or transition metal based oxides, nitrides and oxynitrides.^{8–10} Particularly, titanium nitride (TiN) has recently been investigated as electrocatalyst support materials for both the cathodic oxygen reduction reaction (ORR)¹¹ and anodic

methanol oxidation reaction (MOR),^{12–14} owing to its exemplary chemical and thermal resistance combined with high electronic conductivity. These investigations are generally limited to pure TiN in nanoparticle or thin film morphologies.

The present study highlights the development of novel coaxial TiN coated carbon nanotubes (CNTs) formed by a simplistic two step approach. In the first step, CNTs are utilized as a substrate for the deposition of a layer of titanium dioxide (TiO₂) by a solvothermal procedure. After annealing in argon, the second step involved heat treatment of the TiO₂ coated CNTs under flowing ammonia, resulting in TiN coated CNT (TiN–CNT) composites. These newly developed materials were used as electrocatalyst supports for PEMFC applications by depositing platinum nanoparticles on their surface (Pt/TiN–CNTs). The advantages of using TiN–CNT nanocomposites as electrocatalyst supports for fuel cell reactions are immense. The CNT core structure can effectively provide interconnected electronically conductive pathways^{15,16} during fuel cell operation. They also possess a one-dimensional anisotropic morphology that has been shown to result in enhanced electron transport properties for electrocatalyst materials,¹⁷ can serve to enhance mass transport properties¹⁸ and can easily be arranged into porous, interconnected electrode structures.^{19,20} The TiN coating can further provide a protective barrier in order to hinder the rates of carbon corrosion during fuel cell operation and upon compositing with CNTs has also been shown to result in dramatically enhanced electronic properties compared with pure TiN.^{21,22} Moreover, and most notably, TiN has been found to offer advantageous catalyst–support interactions, including enhanced ORR and MOR kinetics,^{11–14} along with markedly improved CO tolerance towards the MOR.^{13,14} The latter is particularly important in the

Department of Chemical Engineering, Waterloo Institute of Nanotechnology, Waterloo Institute for Sustainable Energy, University of Waterloo, 200 University Avenue West, Waterloo, Ontario, Canada N2L 3G1. E-mail: zhwen@uwaterloo.ca; Fax: +1 519 746 4979; Tel: +1 519 888 4567 ext. 38664

design and development of MOR electrocatalyst materials, as adsorbed CO intermediates will block methanol reactants from the active site moieties,²³ generally overcome by alloying platinum electrocatalyst materials with ruthenium (PtRu). Unfortunately, this bears with it high costs and performance loss arising from the instability of this noble metal.²⁴ Therefore, in the present study, coaxial TiN–CNT composites are developed in order to exploit the distinct advantages of utilizing this novel nanocomposite arrangement as electrocatalyst supports. Using these Pt/TiN–CNT materials, exemplary ORR and MOR performance and electrokinetics were observed, superior to state of the art carbon supported platinum (Pt/C) catalyst. Thus, in the present study TiN–CNT core–shell nanocomposites are presented as promising electrocatalyst support alternatives for low temperature fuel cell applications.

Experimental

Carboxylic acid (0.5%) functionalized CNTs were purchased from a commercial supplier for use in this study. The first step of TiN–CNT synthesis involved the deposition of a TiO₂ layer onto CNT substrates by a simple chemical method modified from a procedure reported previously.²⁵ Briefly, the commercial CNTs were refluxed in 6 M HNO₃ solution for 5 hours to further oxidize the surface of the CNTs in order to provide facile precursor adsorption, remove any amorphous impurities and allow for easier dispersion in solution during processing. Following filtration and washing, 50 mg of the acid treated CNTs were ultrasonically dispersed in 60 mL of ethanol for several hours. The mixture was then transferred to a stir plate and 500 μ L of titanium butoxide was added and allowed to mix constantly for approximately 30 minutes, upon which 500 μ L of DDI water was added and allowed to mix for another 30 minutes. The entire mixture was then refluxed for 6 hours where deposition of the TiO₂ precursors occurred on the surface of the CNTs. After cooling, the products were filtered, washed and annealed under nitrogen protection at 400 °C for 4 hours. Heat treatment in ammonia gas was then carried out in order to allow the conversion of TiO₂ to TiN.^{12,21,22} The temperature was ramped up to 800 °C over 45 minutes under nitrogen protection. After reaching the desired reaction temperature, ammonia was emitted to the system (100 sccm) where the reaction was carried out for 4 hours. After completion, the system was purged with nitrogen and allowed to cool and the TiN–CNT composites could be collected.

Pt nanoparticle deposition onto the surface of TiN–CNTs was carried out by the well established ethylene glycol (EG) reduction method.^{4,8,26,27} Specifically, TiN–CNTs were ultrasonically dispersed in EG solvent, followed by the addition of the required amount of Pt (20 wt%) in the form of a H₂PtCl₆/EG mixture (5 mg Pt mL⁻¹). Under constant stirring, a 2.5 M NaOH/EG solution was added to increase the pH of the solution to *ca.* 13 and then reduction was carried out by refluxing the solution at 140 °C for 3 hours. After cooling the mixture, 1 M aqueous HCl solution was added to reduce the pH to *ca.* 5, followed by filtration and washing of the resulting products.

The materials utilized in this work were characterized by a number of different techniques in order to provide insight into their structure and chemical compositions. Transmission

electron microscopy (TEM) images were obtained using a JEOL 2010F TEM. X-Ray diffraction (XRD) patterns were collected in order to investigate the crystalline structure of the composite support materials. Thermogravimetric analysis (TGA) was carried out under a steady flow of N₂/air (50/50), where the temperature was maintained at 60 °C for thirty minutes in order to remove any water products followed by increasing the temperature from 60 to 900 °C at a steady rate of 20 °C min⁻¹.

All electrochemical characterization was carried out using a three neck glass cell using a CHI electrochemical workstation potentiostat and a Pine electrode rotator. A glassy carbon disk working electrode, platinum wire counter electrode and dual chamber Ag/AgCl reference electrode were utilized for all testing. Where appropriate, electrode potentials were converted to RHE for ease of comparison. Catalyst ink was prepared by mixing 4 mg of catalyst sample into 2 mL of an ethanol/water solution. The sample was ultrasonicated for one hour in order to ensure good dispersion, upon which a 20 μ L aliquot was deposited onto the glassy carbon working electrode. After drying, 10 μ L of a 0.05 wt% Nafion solution was coated onto the electrode in order to ensure adequate adhesion of catalyst sample. Cyclic voltammetry (CV) and ORR testing were carried out in 0.1 M HClO₄. CV was carried out under nitrogen saturation between 0.05 and 1.25 V *vs.* RHE at a scan rate of 50 mV s⁻¹ and no electrode rotation. ORR linear potential sweeps were carried out under oxygen saturated electrolyte conditions at a scan rate of 10 mV s⁻¹ at various electrode rotation speeds (100, 400, 900 and 1600 rpm) in order to provide insight into the electrokinetics of the ORR occurring on the catalyst samples. Background currents obtained under nitrogen saturation were removed in order to eliminate capacitance and redox contributions. MOR testing was carried out in 0.1 M HClO₄ containing 1 M methanol under nitrogen saturation between 0.05 and 1.25 V *vs.* RHE at a scan rate of 5 mV s⁻¹. Chronoamperometry current–time transients were obtained under the same conditions by stepping and holding the electrode potential at 0.82 V *vs.* RHE. Comparison of the electrochemical activity of the developed electrocatalyst materials is made with commercial, 20 wt% platinum nanoparticles supported on carbon black (Pt/C, BASF), a commonly utilized benchmark catalyst. Throughout all electrochemical testing, platinum loading on the electrode was kept the same and current densities are reported on the basis of electrode area (0.19635 cm²).

Results and discussion

The structural evolutions occurring during synthesis of the TiN–CNT composite materials are summarized by the TEM images displayed in Fig. 1. Fig. 1a demonstrates the standard one-dimensional morphology of the acid treated CNTs utilized as substrates for TiN coating. The deposition of TiO₂ on the surface of the CNTs was found to be very uniform as displayed in Fig. 1b, with some small portions of the CNT surface exposed. The polycrystalline TiO₂ shell structure was observed to have a thickness of *ca.* 15–30 nm. Following heat treatment in ammonia, Fig. 1c displays the one-dimensional TiN–CNT coaxial core–shell structure arrangement that is pertinent to this work. A distinct structural transformation was observed for the TiN–CNT composite materials resulting from the conversion of

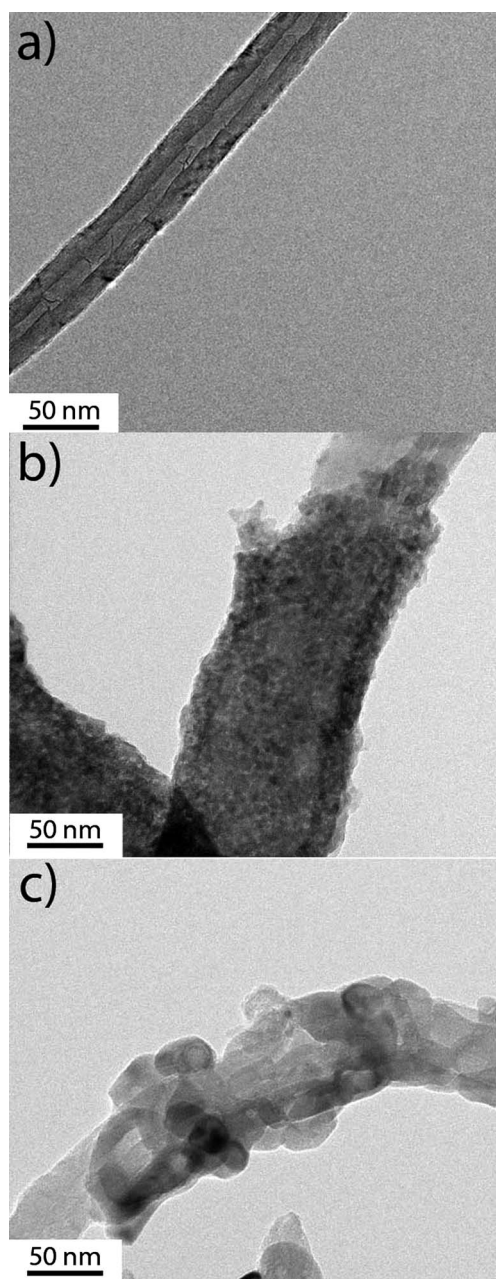


Fig. 1 TEM images of (a) acid treated CNTs, (b) TiO_2 -CNT and (c) TiN-CNT composite materials.

TiO_2 to TiN. The coating layer maintained its thickness and uniformity; however, it exhibited a polycrystalline morphology with larger crystallite sizes compared with the TiO_2 coating layer.

XRD patterns were obtained to provide further insight into the structural transformations occurring during the material synthesis and are displayed in Fig. 2a. TiO_2 -CNT displayed characteristic TiO_2 peaks containing primarily the anatase phase, with a diffraction pattern almost identical to that reported previously for similar materials.²⁵ After heat treatment in ammonia, conversion of TiO_2 to TiN is exclusively confirmed by the distinct shift observed in the diffraction patterns. The peaks are characteristic of TiN materials located at 2θ values of *ca.* 36.7, 42.7, 62.0, 74.8 and 78.0° and can be attributed to the (111), (200), (220), (311) and (222) hexagonal TiN crystal phases,

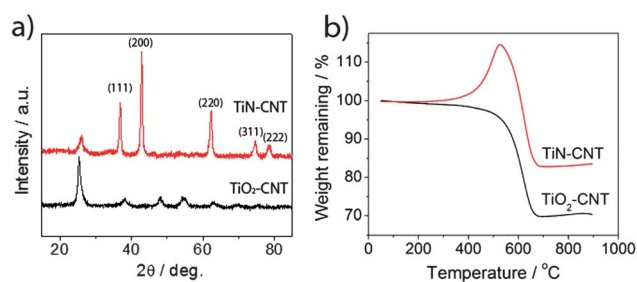


Fig. 2 (a) XRD patterns and (b) TGA profile obtained for TiO_2 -CNT and TiN-CNT composite materials.

respectively. XRD also indicated preservation of the CNT core structure, where the sharp graphitic peak observed at 26° is maintained, corresponding to the (002) plane structure.

TGA profiles obtained for TiO_2 -CNTs and TiN-CNTs and are displayed in Fig. 2b. For the TiO_2 -CNT materials, the TiO_2 shell was determined to comprise *ca.* 70 wt% of the overall composite materials based on the residual mass from TGA testing. Assuming stoichiometric TiO_2 , this represents a very high (>90%) product yield of titanium from the precursor solution, most likely attributed to the high concentration of CNTs present in the reflux mixture and the high degree of functional groups on their surface to readily facilitate precursor adsorption. Mass loss was observed to occur beginning at *ca.* 350 °C, attributed at first to combustion of any amorphous carbon species followed by the CNT core structures. The TGA profile of TiN-CNTs displayed a weight increase initiating at *ca.* 350 °C and reaching a maximum of 114.6 wt% at 525 °C. This increase in weight can be directly attributed to the oxidation of TiN and is in direct agreement with previous reports.²⁸ The weight gain resulting from TiN oxidation is well below the theoretical value of 29.1 wt% assuming complete conversion of stoichiometric TiN to TiO_2 . Non-stoichiometric TiN and TiO_2 offer reasonable explanation for this observation along with the onset of CNT oxidation occurring at these excessive temperatures. The residual mass remaining after completion of the temperature ramping was higher for TiN-CNTs compared with TiO_2 -CNTs, with 83.6 and 70.4 wt% remaining, respectively. Non-stoichiometric TiN and TiO_2 will most likely contribute to this observation; however, it is most likely that the increased residual weight remaining for TiN-CNTs is due to the etching of carbon from the CNTs occurring during ammonia treatment.^{29,30}

Following Pt deposition by a modified ethylene glycol reduction method, TEM imaging (Fig. 3) confirmed the successful deposition of well dispersed Pt nanoparticles with an average diameter of *ca.* 2.9 nm and the majority of nanoparticles possessing diameters between 1 and 4 nm based on measurement of numerous TEM images. This positively indicates that the ethylene glycol method is effective for deposition onto TiN based supports; however, some larger Pt nanoparticle agglomerates were observed, possibly due to the lack of surface functional groups such as the ones on carbon based supports in order to facilitate Pt ion nucleation and subsequent particle growth.^{31,32} The structural morphology of the TiN-CNTs is maintained, with Pt nanoparticles observed on the surface, along with Pt deposition onto the exposed CNT surfaces adjacent to the termination sites of the TiN coating.

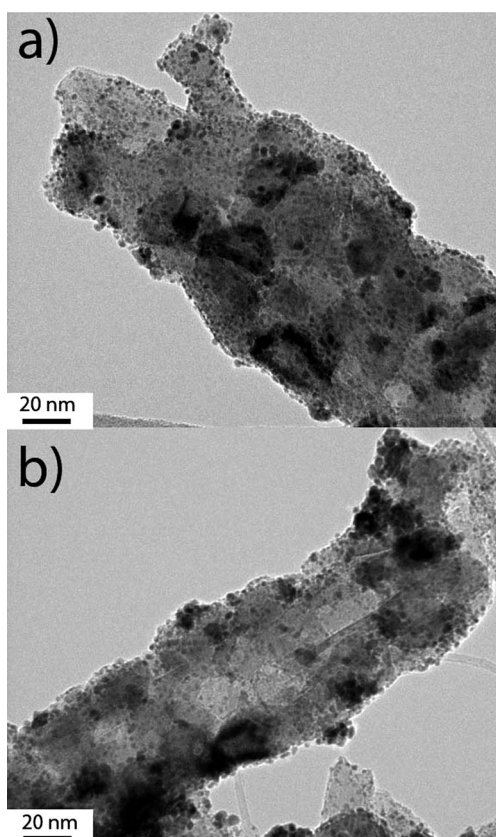


Fig. 3 TEM images of Pt/TiN-CNT composite materials.

CV curves are presented for Pt/TiN-CNTs along with state of the art commercial Pt/C for comparison in Fig. 4a. As expected, both samples display the characteristic platinum oxidation/reduction peaks at higher electrode potentials and the hydrogen adsorption/desorption peaks at lower potentials. The charge transfer for hydrogen desorption was used to calculate the electrochemically active surface area (ECSA) according to eqn (1):³³

$$\text{ECSA} = \frac{Q_{\text{H}}}{[\text{Pt}] \times 0.21} \quad (1)$$

where Q_{H} is the calculated charge for hydrogen desorption (mC cm^{-2}), $[\text{Pt}]$ is the platinum mass based electrode loading ($\text{mg}_{\text{Pt}} \text{cm}^{-2}$) and 0.21 mC cm^{-2} is the charge transfer required for a monolayer of hydrogen on platinum. Based on these calculations, the ECSA of Pt/TiN-CNT was found to be $109.75 \text{ m}^2 \text{ g}_{\text{Pt}}^{-1}$, comparable to $104.37 \text{ m}^2 \text{ g}_{\text{Pt}}^{-1}$ determined for commercial Pt/C.

ORR polarization curves obtained in oxygen saturated 0.1 M HClO_4 are provided in Fig. 4b comparing Pt/TiN-CNTs and commercial Pt/C, along with full polarization curves provided in Fig. 4c and d, respectively. It is apparent that utilizing TiN-CNTs as a catalyst support material enhances the ORR electrokinetics compared with the benchmark state of the art Pt/C electrocatalyst. Improved onset potential and current densities were obtained over the potential range investigated, with a slightly higher diffusion limited current observed. The latter can most likely be attributed to reduced peroxide byproducts released from the carbon support materials due to the TiN shell

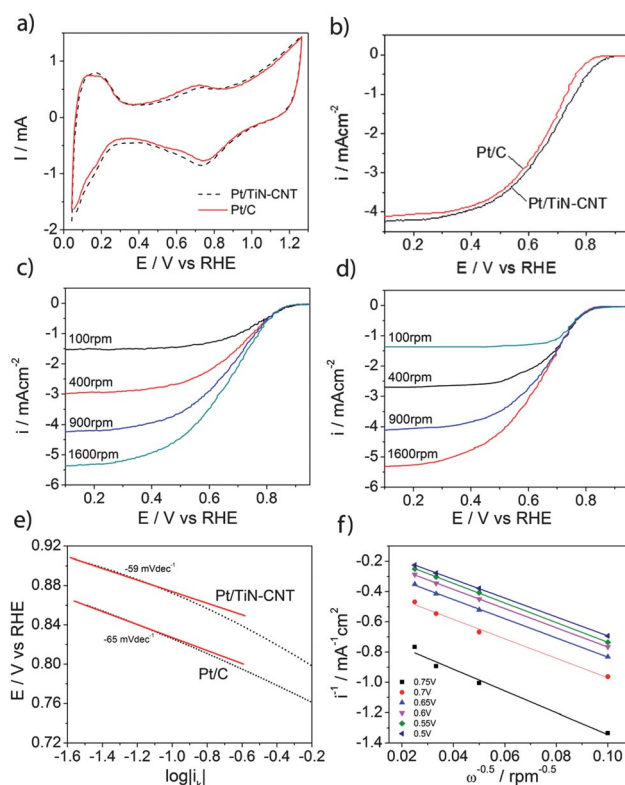


Fig. 4 (a) CV curves for Pt/TiN-CNT and Pt/C obtained in 0.1 M HClO_4 at a scan rate of 50 mV s^{-1} under nitrogen saturation and (b) ORR polarization curves obtained at a scan rate of 10 mV s^{-1} and an electrode rotation rate of 900 rpm under oxygen saturation, with background currents obtained under nitrogen saturation removed. Polarization curves at various rotation rates for (c) Pt/TiN-CNT and (d) Pt/C. (e) Tafel plots for Pt/TiN-CNT and Pt/C (900 rpm) and (f) Koutecky-Levich plots for Pt/TiN-CNTs at various potentials. Identical platinum electrode loading was utilized for all testing.

coating. This higher diffusion limited current density is in contrast to results reported previously indicating a lower diffusion limited current reported for Pt supported on TiN particles compared with Pt/C,¹¹ indicating a potential influence induced by the 1D anisotropic morphology of the TiN-CNTs, or a potential composite interaction with the highly graphitic CNT core supports. Regardless, the improved on-set potential obtained with TiN based catalyst supports is consistent with this previous report, rendering these materials as promising electrocatalyst support materials. Kinetic controlled current densities were determined and Tafel plots of Pt/TiN-CNTs and Pt/C are provided in Fig. 4e. In the low current density region, Tafel slopes of -59 mV dec^{-1} and -65 mV dec^{-1} were observed for Pt/TiN-CNT and Pt/C respectively. This analysis indicates the enhanced ORR electrokinetics occurring on the surface of Pt/TiN-CNTs and the values obtained are very similar to the theoretical low current density Tafel slope of -60 mV dec^{-1} commonly reported for platinum materials in the cathodic sweep direction.^{34,35} At higher current density values, a shift in the slope is observed to more negative values commonly attributed to altered adsorption isotherms and reaction mechanisms.^{36,37} Fig. 4f exhibits Koutecky-Levich plots for Pt/TiN-CNTs at various potentials in the mixed diffusion-kinetic current density

regime. Parallel, linear behaviour is observed which confirms first order reaction kinetics with respect to oxygen concentration occurring on the Pt/TiN–CNT electrode.³⁸ It has however, recently been demonstrated that upon immersion in acidic solutions and exposure to potential cycling over long periods of time the surface of TiN will be passivated, ultimately resulting in drastic performance loss.³⁹ It is unknown how this reported phenomenon will behave under actual fuel cell conditions and remains to be investigated; however, this surface passivation is an implicit drawback of TiN based support materials that must be overcome in order to exploit their significant electrokinetic enhancements as ORR electrocatalyst supports. Future investigations on this phenomenon would be beneficial.

CV curves obtained in 0.1 M HClO₄ containing 1 M methanol are presented in Fig. 5a for Pt/TiN–CNTs and Pt/C. Pt/TiN–CNTs demonstrated superior MOR activity, displaying a forward peak current density of 22.9 mA cm⁻², compared to 15.8 mA cm⁻² observed for commercial Pt/C. Along with a slightly improved on-set potential and significantly higher oxidation currents obtained throughout the entire potential range investigated, Pt/TiN–CNTs also displayed higher resistance to CO poisoning. CO poisoning is a primary concern for MOR electrocatalyst development, as adsorbed CO intermediates will serve to block methanol access to the catalytically active sites, reducing the overall rate of electrochemical oxidation. Generally, the forward peak current density (i_f) is attributed to the oxidation of methanol and the backward peak current density (i_b) is attributed to the oxidation of adsorbed CO species. Improved forward peak to backward peak current density ratios (i_f/i_b) are indicative of enhanced electrocatalyst tolerance towards CO poisoning. Alloying platinum with ruthenium is a well accepted strategy to mitigate the effects of CO poisoning, where improved MOR performance is commonly reported for PtRu alloy electrocatalysts.^{23,24,40} This strategy however relies exclusively on ruthenium supplies, bearing with it the issues of high cost and limited global reserves. Moreover, ruthenium leaching during fuel cell operation can also result in performance loss resulting from the dealloying process along with contamination of fuel cell components by ruthenium ions.^{24,41} In the present study, Pt/TiN–CNTs displayed improved CO tolerance compared with Pt/C, demonstrating i_f/i_b ratios of 1.22 and 1.12, respectively. Chronoamperometry current–time transients are provided in Fig. 5b for Pt/TiN–CNTs and Pt/C by holding the

electrode at a potential of 0.82 V vs. RHE. Higher MOR current densities and reduced rates of current depletion were observed for Pt/TiN–CNTs, further indicative of the superior MOR kinetics and CO tolerance of these materials, respectively.

The performance enhancement observed for Pt/TiN–CNTs can most likely be attributed to the specific properties of the TiN–CNT composites and the catalyst–support interactions present in these materials. Reduced CO poisoning when utilizing TiN supported Pt has been previously reported in both alkaline¹⁴ and acidic environments¹³ and was attributed to the formation of hydroxide groups during potential cycling as confirmed by infrared spectroscopy techniques. These authors claim that CO species adsorbed on active Pt sites will be removed by adjacent hydroxide species present on the TiN support in a fashion similar to the alleviated CO poisoning observed on PtRu alloys due to the presence of Ru–OH groups. This claim has been supported by the increase in MOR activity observed as a function of potential cycling^{13,14} resulting in the formation of TiN–OH species. This observation was also observed in the present study, where performance increase was observed for Pt/TiN–CNTs as a function of potential cycling before steady state current densities were obtained. Additional catalyst–support interactions occurring between the TiN–CNTs and Pt nanoparticles may also account for the enhancements in the performance observed, where electrocatalyst activity is known to be strongly influenced by the type of support material utilized. The possible interactions occurring between TiN–CNTs and the active Pt nanoparticles remain elusive and further investigations are required; however, it has been proposed that there may exist a synergistic mechanism that occurs when the surface of oxidized TiN (oxide or oxynitride species) undergoes reduction, simultaneously mediating the oxidation of methanol molecules.¹³ Moreover, a shift in the electron binding energy of Pt supported on TiN species has been demonstrated by X-ray photoelectron spectroscopy.¹² These modified electron properties could potentially account for improvements in the MOR and ORR electrokinetics observed on Pt/TiN–CNTs in comparison to commercial carbon supported Pt. It is also likely that the improved electronic properties obtained upon compositing TiN materials with CNTs, along with the distinct advantages of using electrocatalysts possessing unique, one dimensional morphologies, will provide electrocatalytic improvements. While the exact nature of the enhancements reported herein requires stringent investigations, the promise of utilizing TiN–CNTs as electrocatalyst support materials is apparent.

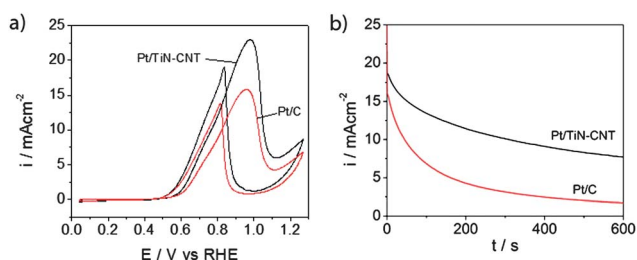


Fig. 5 (a) MOR polarization curves for Pt/TiN–CNT and Pt/C obtained in 0.1 M HClO₄ containing 1 M methanol at a scan rate of 5 mV s⁻¹. (b) Chronoamperometry current–time transients at an electrode potential of 0.82 V vs. RHE. Identical platinum electrode loading was utilized for all testing.

Conclusions

Unique TiN–CNT core–shell nanocomposites were developed by a simplistic fabrication procedure and were characterized by XRD, TGA and TEM techniques. These materials were then utilized as platinum nanoparticle supports for ORR and MOR fuel cell reactions. Improved ORR and MOR activities were obtained for Pt/TiN–CNTs compared with commercial state of the art Pt/C electrocatalysts. Improved CO tolerance of these materials determined through MOR and chronoamperometry testing was also demonstrated. These performance enhancements were attributed to the specific properties of the TiN–CNT nanocomposites, particularly their one-dimensional anisotropic

morphology and improved electronic properties. Moreover, distinct catalyst–support interactions most likely play a role in the electrokinetic enhancements and CO tolerance observed. Thus, TiN–CNTs are presented as promising electrocatalyst support materials for low temperature fuel cell applications.

Acknowledgements

This work was financially supported by the Natural Sciences and Engineering Research Council of Canada (NSERC), the University of Waterloo and the Waterloo Institute for Nanotechnology. TEM images were obtained at the Canadian Centre for Electron Microscopy at McMaster University.

References

- 1 Y. Shao, J. Liu, Y. Wang and Y. Lin, *J. Mater. Chem.*, 2008, **19**, 46–59.
- 2 Y. Qiao and C. M. Li, *J. Mater. Chem.*, 2011, **21**, 4027–4036.
- 3 Y. Chen, J. Wang, H. Liu, R. Li, X. Sun, S. Ye and S. Knights, *Electrochem. Commun.*, 2009, **11**, 2071–2076.
- 4 D. C. Higgins, D. Meza and Z. Chen, *J. Phys. Chem. C*, 2010, **114**, 21982–21988.
- 5 M. S. Saha, R. Li, X. Sun and S. Ye, *Electrochem. Commun.*, 2009, **11**, 438–441.
- 6 L. Dong, R. R. S. Gari, Z. Li, M. M. Craig and S. Hou, *Carbon*, 2010, **48**, 781–787.
- 7 B. Seger and P. V. Kamat, *J. Phys. Chem. C*, 2009, **113**, 7990–7995.
- 8 R. S. Hsu, D. Higgins and Z. Chen, *Nanotechnology*, 2010, **21**, 165705–165810.
- 9 S. Y. Huang, P. Ganesan, S. Park and B. N. Popov, *J. Am. Chem. Soc.*, 2009, **131**, 13898–13899.
- 10 T. Ioroi, Z. Siroma, N. Fujiwara, S. Yamazaki and K. Yasuda, *Electrochem. Commun.*, 2005, **7**, 183–188.
- 11 B. Avasarala, T. Murray, W. Li and P. Haldar, *J. Mater. Chem.*, 2009, **19**, 1803–1805.
- 12 J. M. Lee, S. B. Han, Y. J. Song, J. Y. Kim, B. Roh, I. Hwang, W. Choi and K. W. Park, *Appl. Catal., A*, 2010, **375**, 149–155.
- 13 O. T. M. Musthafa and S. Sampath, *Chem. Commun.*, 2008, 67–69.
- 14 M. M. O. Thotiyl, T. Ravikumar and S. Sampath, *J. Mater. Chem.*, 2010, **20**, 10643–10651.
- 15 E. Hosono, Y. Wang, N. Kida, M. Enomoto, N. Kojima, M. Okubo, H. Matsuda, Y. Saito, T. Kudo and I. Honma, *ACS Appl. Mater. Interfaces*, 2009, **2**, 212–218.
- 16 H. Y. Du, C. H. Wang, H. C. Hsu, S. T. Chang, S. C. Yen, L. C. Chen, B. Viswanathan and K. H. Chen, *J. Mater. Chem.*, 2011, **21**, 2512–2516.
- 17 M. Rauber, I. Alber, S. Müller, R. Neumann, O. Picht, C. Roth, A. Schoekel, M. E. Toimil-Molares and W. Ensinger, *Nano Lett.*, 2011, **6**, 2304–2310.
- 18 Z. Chen, M. Waje, W. Li and Y. Yan, *Angew. Chem.*, 2007, **119**, 4138–4141.
- 19 D. C. Higgins and Z. Chen, *ECS Trans.*, 2010, **28**, 63–68.
- 20 W. Li, X. Wang, Z. Chen, M. Waje and Y. Yan, *Langmuir*, 2005, **21**, 9386–9389.
- 21 L. Jiang and L. Gao, *J. Mater. Chem.*, 2005, **15**, 260–266.
- 22 L. Jiang and L. Gao, *J. Am. Chem. Soc.*, 2006, **89**, 156–161.
- 23 Z. Liu, J. Y. Lee, M. Han, W. Chen and L. M. Gan, *J. Mater. Chem.*, 2002, **12**, 2453–2458.
- 24 P. Piela, C. Eickes, E. Broscha, F. Garzon and P. Zelenay, *J. Electrochem. Soc.*, 2004, **151**, A2053–A2059.
- 25 F. F. Cao, Y. G. Guo, S. F. Zheng, X. L. Wu, L. Y. Jiang, R. R. Bi, L. J. Wan and J. Maier, *Chem. Mater.*, 2010, **22**, 1908–1914.
- 26 Z. Chen, L. Xu, W. Li, M. Waje and Y. Yan, *Nanotechnology*, 2006, **17**, 5254–5259.
- 27 W. Li, M. Waje, Z. Chen, P. Larsen and Y. Yan, *Carbon*, 2010, **48**, 995–1003.
- 28 O. Schulz, N. Eisenreich, H. Fietzek, M. M. Juez Lorenzo and E. Kondratenko, *Part. Part. Syst. Charact.*, 2010, **27**, 58–68.
- 29 F. Jaouen, F. Charretier and J. Dodelet, *J. Electrochem. Soc.*, 2006, **153**, A689–A698.
- 30 F. Jaouen and J. P. Dodelet, *J. Phys. Chem. C*, 2007, **111**, 5963–5970.
- 31 H. Y. Du, C. H. Wang, H. C. Hsu, S. T. Chang, U. S. Chen, S. Yen, L. Chen, H. C. Shih and K. Chen, *Diamond Relat. Mater.*, 2008, **17**, 535–541.
- 32 W. Li, C. Liang, W. Zhou, J. Qiu, Z. Zhou, G. Sun and Q. Xin, *J. Phys. Chem. B*, 2003, **107**, 6292–6299.
- 33 A. Pozio, M. De Francesco, A. Cemmi, F. Cardellini and L. Giorgi, *J. Power Sources*, 2002, **105**, 13–19.
- 34 D. Banham, F. Feng, T. Fürstenthaupt, K. Pei, S. Ye and V. Birss, *J. Power Sources*, 2011, **196**, 5438–5445.
- 35 N. M. Markovic, H. A. Gasteiger and P. N. Ross, Jr, *J. Phys. Chem.*, 1995, **99**, 3411–3415.
- 36 D. Meza, U. Morales, P. Roquero and L. Salgado, *Int. J. Hydrogen Energy*, 2010, **35**, 12111–12114.
- 37 Y. H. Shih, G. V. Sagar and S. D. Lin, *J. Phys. Chem. C*, 2008, **112**, 123–130.
- 38 D. Higgins, Z. Chen and Z. Chen, *Electrochim. Acta*, 2010, **56**, 1570–1575.
- 39 B. Avasarala and P. Haldar, *Electrochim. Acta*, 2010, **55**, 9024–9034.
- 40 F. Muench, S. Kaserer, U. Kunz, I. Svoboda, J. Brötz, S. Lauterbach, H. J. Kleebe, C. Roth and W. Ensinger, *J. Mater. Chem.*, 2011, **21**, 6286–6291.
- 41 W. Chen, G. Sun, J. Guo, X. Zhao, S. Yan, J. Tian, S. Tang, Z. Zhou and Q. Xin, *Electrochim. Acta*, 2006, **51**, 2391–2399.